Giant frequency-selective near-field energy transfer in active–passive structures

Chinmay Khandekar, Weiliang Jin, Owen D. Miller, Adi Pick, and Alejandro W. Rodriguez

Giant frequency-selective near-field energy transfer in active–passive structures

Chinmay Khandekar,[1] Weiliang Jin,[1] Owen D. Miller,[2] Adi Pick,[3] and Alejandro W. Rodriguez[1]

[1]*Department of Electrical Engineering, Princeton University, Princeton, NJ 08544, USA*
[2]*Department of Mathematics, Massachusetts Institute of Technology, Cambridge, MA 02139, USA*
[3]*Department of Physics, Harvard University, Cambridge, MA 02138, USA*

We apply a fluctuation electrodynamics framework in combination with semi-analytical (dipolar) approximations to study amplified spontaneous energy transfer (ASET) between active and passive bodies. We consider near-field energy transfer between semi-infinite planar media and spherical structures (dimers and lattices) subject to gain, and show that the combination of loss compensation and near-field enhancement (achieved by the proximity, enhanced interactions, and tuning of subwavelength resonances) in these structures can result in orders of magnitude ASET enhancements below the lasing threshold. We examine various possible geometric configurations, including realistic materials, and describe optimal conditions for enhancing ASET, showing that the latter depends sensitively on both geometry and gain, enabling efficient and tunable gain-assisted energy extraction from structured surfaces.

Radiative heat transfer between nearby objects can be much larger in the near field (sub-micron separations) than in the far field[1–3] due to coupling between evanescent (surface-localized) waves.[4,5] In this paper, we investigate the possibility of exploiting both active materials and geometry to enhance and tune near-field energy transfer. In particular, we study amplified spontaneous energy transfer (ASET)—the amplified spontaneous emission (ASE) from a gain medium that is absorbed by a nearby passive object—and demonstrate orders of magnitude enhancements compared to far-field emission or transfer between passive structures. Our work extends previous work on heat transfer between planar, passive media[6–9] to consider the possibility of using gain as a mechanism of loss cancellation, leading to further flux-rate enhancements under certain conditions (diverging at the onset of lasing). Since planar structures are known to be sub-optimal near-field energy transmitters,[10] we also consider a more complicated geometry involving subwavelength metallic dimers or lattices of spheres doped with active emitters, and describe conditions under which ASET ≫ ASE below the lasing threshold (LT). Our analysis of these spherical structures includes both semi-analytical calculations (for dimers) and dipolar approximations that include first-order geometric modifications to the polarization response of spheres (for lattices), revealing not only significant potential enhancements but also strongly geometry-dependent variations in ASET stemming from the presence of multiple scattering, which suggests the possibility of using the near field as a mechanism for tuning energy extraction. Similar to our recent findings in the case of passive objects,[11] we find that energy exchange between lattice of spheres tends to greatly outperform exchange between planar bodies as the intrinsic loss rates of materials decrease, with gain contributing additional enhancement.

Recent approaches to tailoring incoherent emission from nanostructured surfaces have begun to explore situations that deviate from the usual linear and passive materials of the past,[12–17] with the majority of these works primarily focusing on ways to control far-field emission, e.g. the lasing properties of active materials.[18] Here we consider a different subset of such systems: structured active–passive bodies that exchange energy among one another more efficiently than they do into the far field. Our predictions below extend recent progress in understanding and tailoring energy exchange between structured materials, which thus far include doped semiconductors,[19] phase-change materials,[20,21] and metallic gratings.[22–24] Active control of near field heat exchange offers a growing number of applications, from heat flux control[25,26] and solid-state cooling[26] to thermal diodes.[27,28] Our work extends these recent ideas to situations involving systems undergoing gain-induced amplification.

The starting point of our analysis is the well-known linear fluctuational electrodynamics framework established by Rytov, Polder, and van Hove.[29,30] In particular, given two bodies held at temperatures T_1 and T_2, and separated by a distance d, the power or heat transfer from $1 \rightarrow 2$ is given by:[4]

$$P(T_1, T_2) = \int_0^\infty [\Theta(\omega, T_1) - \Theta(\omega, T_2)] \Phi_{12}(\omega) \frac{d\omega}{2\pi} \quad (1)$$

where $\Theta(\omega, T)$ is the mean energy of a Planck oscillator at frequency ω and temperature T, and $\Phi_{12}(\omega)$ denotes the spectral radiative heat flux, or the absorbed power in object 2 due to spatially incoherent dipole currents in 1. Such an expression is often derived by application of the fluctuation-dissipation theorem (FDT), which relates the spectral density of current fluctuations in the system to dissipation,[4] $\langle J_i(\mathbf{x}, \omega), J_j^*(\mathbf{x}', \omega) \rangle = \frac{4}{\pi} \omega \epsilon_0 \, \text{Im} \, \epsilon(\mathbf{x}, \omega) \delta(\mathbf{x} - \mathbf{x}') \Theta(\omega, T) \delta_{ij}$, where J_i denotes the current density in the ith direction, ϵ_0 and $\epsilon(\mathbf{x}, \omega)$ are the vacuum and relative permittivities at $\mathbf{x}$, and $\langle \cdots \rangle$ denotes a thermodynamic ensemble-average.

Extensions of the FDT above to situations involving active media require macroscopic descriptions of their dielectric response. Below, we consider an atomically doped gain medium that, ignoring stimulated emission or nonlinear effects arising above threshold,[31] can be accurately modelled (under the stationary-inversion approximation) by a simple two-level Lorentzian gain profile of the atomic populations n_1 and n_2, resulting in the following effective permittivity:[32]

$$\epsilon(\omega) = \epsilon_r(\omega) + \underbrace{\frac{4\pi g^2}{\hbar \gamma_\perp} \frac{\gamma_\perp D_0}{\omega - \omega_{21} + i\gamma_\perp}}_{\epsilon_G(\omega)} \quad (2)$$

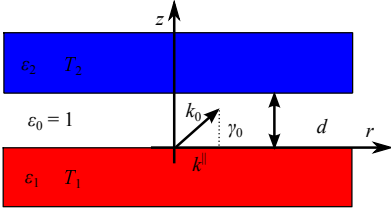where ϵ_r denotes the permittivity of the background medium and the second term describes the gain profile ϵ_G, which

FIG. 1. Schematic of two semi-infinite plates of permittivities ϵ_1 and ϵ_2, respectively, separated by a vacuum gap d. Fourier decomposition of scattered waves with respect to parallel $k_\parallel$ and perpendicular γ wavevectors simplifies calculations of energy transfer.

depends on the "lasing" frequency ω_{21}, polarization decay rate $\gamma_\perp$, coupling strength g, and population inversion $D_0 = n_2 - n_1$ associated with the $2 \to 1$ transition. Detailed-balance and thermodynamic considerations lead to a modified version of the FDT[31,33,34] involving an effective Planck distribution $\Theta(\omega_{21}, T_G) = -n_2 \hbar \omega_{21}/D_0$, in which case the system exhibits a negative effective or "dynamic" temperature under $n_2 > n_1$.[34] Note that even though $\Theta < 0$ under population inversion, the radiation from such a medium is positive-definite: because $\mathrm{Im}\,\epsilon_G < 0$, the spectral correlations associated with the active medium,

$$\langle J_i(\mathbf{x}, \omega) J_j^*(\mathbf{x}', \omega) \rangle = -\frac{4}{\pi} \omega \epsilon_0 (\mathrm{Im}\,\epsilon_G) \underbrace{n_2 \hbar \omega_{21}/D_0}_{\Theta(\omega_{21}, T_G)} \quad (3)$$

are positive-definite. As a consequence, the heat transfer originating from atomic fluctuations in an active body to a passive body always flows from the former to the latter, i.e. $T < 0$ reservoirs always transfer energy.[31] Of course, in addition to fluctuations of the polarization of the gain atoms, such a medium will also exhibit fluctuations in the polarization of the host medium, depending on its thermodynamic temperature and background loss rate $\sim \mathrm{Im}\,\varepsilon_r$, as described by the standard FDT.[4] Although thermal flux rates can themselves be altered (e.g. enhanced) in the presence of gain through the dependence of Φ_{12} on the overall permittivity, the flux rate from such an active medium will tend to be dominated by the fluctuations of the gain atoms, the focus of our work.

I. PLANAR MEDIA

We begin our analysis of ASET by first considering an extensively studied geometry involving two semi-infinite plates that exchange energy in the near field. Such a situation has been thoroughly studied in the past in various contexts,[6–9] but with passive materials, whereas below we consider the possibility of optical gain in one of the plates. For simplicity, we omit the frequency dependence in the complex dielectric functions ϵ_j of the two plates ($j = 1, 2$), shown schematically in Fig. 1 along with our chosen coordinate convention. We assume that one of the plates is doped with a gain medium, such that $\epsilon_1 = \epsilon_r + \epsilon_G$, and consider only fluxes due to fluctuations in the active constituents $\sim \mathrm{Im}\,\epsilon_G$, as described by the modified FDT above.[4,35] Due to the translational symmetry of the

system, it is natural to express the heat flux in a Fourier basis of propagating transverse waves $k_\parallel$,[4] in which case the flux is given by an integral $\Phi(\omega) = \int \Phi(\omega, k_\parallel) k_\parallel dk_\parallel$. In the near field, $k_\parallel > \omega/c$, the main contributions to the integrand come from evanescent waves which exchange energy at a rate,[5,29]

$$\Phi_{12}(\omega, k_\parallel) \approx \sum_{q=s,p} \frac{\mathrm{Im}(\epsilon_G) \, \mathrm{Im}(r_1^q) \, \mathrm{Im}(r_2^q) e^{-2\,\mathrm{Im}(\gamma_0) d}}{\mathrm{Im}\,\epsilon_1 \left| 1 - r_1^q r_2^q e^{-2\,\mathrm{Im}(\gamma_0) d} \right|^2}, \quad (4)$$

where $r_j^s = \frac{\gamma_0 - \gamma_j}{\gamma_0 + \gamma_j}$ and $r_j^p = \frac{\epsilon_j \gamma_0 - \gamma_j}{\epsilon_j \gamma_0 + \gamma_j}$ are the Fresnel reflection coefficients at the interface between vacuum and the dielectric media, for s and p polarizations, respectively, defined in terms of the wavevectors $\mathbf{k}_j = k_\parallel \hat{\mathbf{r}} + \gamma_j \hat{\mathbf{z}}$, with $|\mathbf{k}_0| = \omega/c$ and $|\mathbf{k}_j|^2 = k_\parallel^2 + \gamma_j^2 = \sqrt{\epsilon_j} \omega/c$. Note that the derivation of Fresnel coefficients requires special care since when gain compensates loss, i.e. $\mathrm{Im}\,\epsilon_1 < 0$, the sign of the perpendicular wavevector $\gamma_1 = \pm\sqrt{\epsilon_1 \omega^2/c^2 - k_\parallel^2}$ needs to be chosen correctly inside the gain medium.[36–38] Here, we make the physically motivated choice that yields decaying surface waves inside the semi-infinite gain medium. In the case of evanescent waves $k_\parallel \gg \omega/c$, $\gamma_0 \approx \gamma_j \approx ik_\parallel$, such that $r_j^s \to 0$ and $r_j^p = \frac{\epsilon_j - 1}{\epsilon_j + 1} = \frac{|\epsilon_j|^2 - 1}{|\epsilon_j + 1|^2} + \frac{2\epsilon_j'' i}{|\epsilon_j + 1|^2}$, where $\epsilon_j = \epsilon_j' + i\epsilon_j''$. Substituting $e^{2k_\parallel d} = z$ and approximating the integral $\int z f(z) dz \approx z_0 f(z)$, with $z_0 = k_0 d = \ln |r_1^p r_2^p|$ denoting the wavevector that minimizes the denominator of (4), one obtains:

$$\Phi_{12}(\omega) = \frac{z_0 \, \mathrm{Im}(\epsilon_G) \, \mathrm{Im}(r_1^p) \, \mathrm{Im}(r_2^p)}{4\pi^2 d^2 \, \mathrm{Im}\,\epsilon_1}$$
$$\times \int_1^\infty \frac{dz}{(z - \mathrm{Re}(r_1^p r_2^p))^2 + (\mathrm{Im}(r_1^p r_2^p))^2} \quad (5)$$

It follows that the flux rate in the case of passive media with small loss rates scales as $\Phi_{12} \approx \ln |r_1^p r_2^p|/(4\pi^2 d^2) \sim \frac{1}{d^2} \ln |\frac{\epsilon_1 - 1}{\mathrm{Im}\,\epsilon_1} \frac{\epsilon_2 - 1}{\mathrm{Im}\,\epsilon_2}|$ under the resonant condition $\mathrm{Re}\,\epsilon_j = -1$, illustrating a slow, logarithmic dependence on the loss rates and corresponding divergence as $\mathrm{Im}\,\epsilon_j \to 0$, described in Ref. 11. However, ASET in the presence of gain, described by (5), depends differently on the loss rates. On the one hand, in situations where gain does not compensate for losses ($\mathrm{Im}\,\epsilon_1 > 0$), the integral can be further simplified to yield $\Phi_{12} \approx \frac{1}{d^2} \frac{\mathrm{Im}\,\epsilon_G}{\mathrm{Im}\,\epsilon_1} \ln |\frac{\epsilon_1 - 1}{\mathrm{Im}\,\epsilon_1} \frac{\epsilon_2 - 1}{\mathrm{Im}\,\epsilon_2}|$, illustrating the same logarithmic dependence on loss rates and resonant conditions, but with the flux rate exhibiting an additional factor $\sim \mathrm{Im}\,\epsilon_G/\mathrm{Im}\,\epsilon_1$. On the other hand, when the active plate has overall gain, i.e. $\mathrm{Im}\,\epsilon_1 < 0$, the integral diverges under the modified condition $\mathrm{Re}(r_1^p r_2^p) > 1$ and $\mathrm{Im}(r_1^p r_2^p) = 0$, or alternatively,

$$(|\epsilon_1|^2 - 1)(|\epsilon_2|^2 - 1) - 4\epsilon_1'' \epsilon_2'' > |\epsilon_1 + 1|^2 |\epsilon_2 + 1|^2 \quad (6)$$
$$\epsilon_2''(|\epsilon_1|^2 - 1) + \epsilon_1''(|\epsilon_2|^2 - 1) = 0 \quad (7)$$

both of which cannot be simultaneously satisfied below threshold. Note that in this regime, $\mathrm{Re}\,\epsilon = -1$ is no longer a necessary condition for maximum heat transfer. In particular, the divergence can occur at unequal values of $\mathrm{Re}\,\epsilon_j$ and $\mathrm{Im}\,\epsilon_j$,
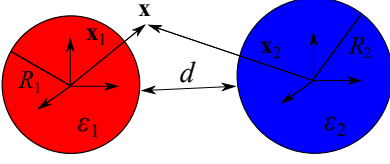
FIG. 2. Schematic of dimer system consisting of two spheres of permittivities ϵ_1 and ϵ_2 and radii R_1 and R_2, respectively, and separated by a gap d. Mie-series decomposition of scattered fields simplifies calculations of energy transfer; shown are a flux evaluation point $\mathbf{x} = \mathbf{x}_1 = \mathbf{x}_2$ in medium 0, with $\mathbf{x}_i$, denoting the position relative to the center of sphere i.

in which case the linewidth $\sim |\operatorname{Im}(r_1^p r_2^p)|$ and peak wavevector $\sim \operatorname{Re}(r_1^p r_2^p)$ are decreased and increased, respectively, by suitable choices of material parameters. Such a divergence is of course indicative of a LT, at which point linear fluctuational electrodynamics is no longer valid. Although semi-infinite plates offer analytical insights and computational ease, their closed nature and large effective loss rates make them far from ideal for studying ASET. In what follows, we consider finite and open geometries in which even larger ASET and tunability can be attained.

II. SPHERE DIMERS AND LATTICES

A. Sphere dimers

Consider an illustrative open geometry consisting of two spheres separated by vacuum, shown in Fig. 2. In addition to material loss, such a system also suffers from radiative losses, which we quantify (neglecting stimulated emission) from the far-field flux Φ_0. The calculation of heat transfer between two spheres was only recently carried out using both semi-analytical[8] and brute-force methods.[39] Here, we extend these studies to consider far-field radiation from one of the spheres (in the presence of the other) and the possibility of gain. In particular, we analyze the near-field energy exchange Φ_{12} and far field emission Φ_0 by exploiting a semi-analytical method (SA) based on Mie-series expansion of scattered waves, and which follows from a recent study of heat transfer in an equivalent but passive geometry.[8]

Due to the spherical symmetry of each object, it is natural to consider scattering in this system by employing field expansions in terms of Mie series.[40] Figure 2 shows a schematic of the system, consisting of two vacuum-separated spheres of radii R_j and dielectric permittivities ϵ_j, separated by surface–surface distance d, where one of the spheres is doped with a gain medium, such that $\epsilon_1 = \epsilon_r + \epsilon_G$. We compute the flux rates through a surface S in vacuum from dipoles $\mathbf{x}_1' \in V_1$ which is given by $\operatorname{Re} \oint_S \langle \mathbf{E}^* \times \mathbf{H} \rangle = \frac{\omega^2 \operatorname{Im} \epsilon_G}{\pi} \operatorname{Im} \oint_S \int_{V_1} d^3 \mathbf{x}_1' \, \mathbb{G}^* \times (\nabla \times \mathbb{G}) \cdot d\mathbf{S}$, where $\mathbb{G}(\mathbf{x}, \mathbf{x}_1')$ is the Dyadic Green's function (GF), or the electric field due to a dipole source at $\mathbf{x}_1'$ evaluated at a point $\mathbf{x} = \mathbf{x}_1 = \mathbf{x}_2$ in vacuum, with $\mathbf{x}_j$ denoting the position relative to the center of sphere j, and where we have employed

the FDT above to express the flux as a sum of contributions from individual (spatially uncorrelated) dipoles.

When expressed in a basis of Mie modes, the GF from a dipole at a position $\mathbf{x}_1' \in V_1$ evaluated at $\mathbf{x}$ is given by:[8]

$$
\mathbb{G}(\mathbf{x}, \mathbf{x}_1') = ik_0 \sum_{\substack{\ell,\nu=(1,m) \\ m=-N}}^{\substack{\ell,\nu=N \\ m=N}} (-1)^m \sum_{q,q'=\pm} \mathbf{M}_{\ell,-m}^{(1)q'}(k_1 \mathbf{x}_1') \otimes
$$
$$
\left[C_{\nu m}^{\ell q q'} \mathbf{M}_{\nu m}^{(3)q}(k_0 \mathbf{x}_1) + D_{\nu m}^{\ell q q'} \mathbf{M}_{\nu m}^{(3)q}(k_0 \mathbf{x}_2) \right], \quad (8)
$$

where $k_j = \sqrt{\epsilon_j}\omega/c$, $\ell \in \mathbb{Z}^+$, $|m| \le \ell$, N denotes the maximum Mie order, $C_{\nu m}^{\ell q q'}$ and $D_{\nu m}^{\ell q q'}$ are standard Mie coefficients,[40,41] $\mathbf{M}_{\ell m}^{(p)\pm}$ denote spherical vector waves, $z_\ell^{(p)}$ are spherical Bessel ($p=1$) and Hankel ($p=3$) functions of order ℓ, $\zeta_\ell^{(p)}(x) = \frac{1}{x}\frac{d}{dx}[x z_\ell^{(p)}(x)]$, and $\mathbf{V}_{\ell m}^{(p)}$ are spherical vector harmonics.[42]

The advantages of employing spherical vector waves comes from the useful orthogonality relations[8] described in Appendix A, which greatly simplify the calculation of fluxes, requiring integration over V_1 and over either the surface $S : |\mathbf{x}_2| \to R_2$ circumscribing sphere 2 (as derived previously in Ref. 8) or a far-away surface $S : |\mathbf{x}| \to \infty$, leading to the following expressions:

$$
\Phi_{12}(\omega) = \frac{R_1 \operatorname{Im} \epsilon_G}{R_2 \operatorname{Im} \epsilon_1} \sum_{\substack{m,\ell,\nu \\ q,p=\pm}} \operatorname{Im}\left(\frac{1}{x_\nu^q(R_2)}\right) \operatorname{Im}\left(\frac{1}{x_\ell^p(R_1)}\right)
$$
$$
\times \left| \frac{z_\ell^{(1)}(k_1 R_1) D_{\nu m}^{\ell q p}}{z_\nu^{(1)}(k_0 R_2)} \right|^2 |x_\ell^p(R_2)|^2, \quad (9)
$$

$$
\Phi_0(\omega) = \frac{2k_0^3 R_1^2 \operatorname{Im} \epsilon_G}{\pi \operatorname{Im} \epsilon_1} \sum_{\substack{m,l,\nu \\ q,p=\pm}} y_\ell^p(R_1) \left(|D_{\nu m}^{\ell q p}|^2 + |C_{\nu m}^{\ell q p}|^2 \right),
$$
$$
(10)
$$

where $C_{\nu m}^{\ell q q'}$ and $D_{\nu m}^{\ell q q'}$ are so-called Mie coefficients,[40]

$$
x_\nu^+(r) = k_0 r \zeta_\nu^{(1)}(k_1 r) z_\nu^{(1)}(k_0 r) - k_1 r \zeta_\nu^{(1)}(k_0 r) z_\nu^{(1)}(k_1 r)
$$
$$
y_\nu^+(r) = \lim_{R \to \infty} R^2 \operatorname{Im}[z_\nu^{(3)}(k_0 R) \zeta_\nu^{(3)*}(k_0 R)]
$$
$$
\times \operatorname{Im}[z_\nu^{(1)}(k_1 r) \zeta_\nu^{(1)*}(k_1 r)],
$$

$x_\nu^-(r) = x_\nu^+(r|\zeta \leftrightarrow z)$, $y_\nu^-(r) = y_\nu^+(r|\zeta \leftrightarrow z)$, $z_\ell^{(p)}$ are spherical Bessel ($p=1$) and Hankel ($p=3$) functions of order ℓ, $\zeta_\ell^{(p)}(x) = \frac{1}{x}\frac{d}{dx}[x z_\ell^{(p)}(x)]$, and $k_j = \omega\sqrt{\epsilon_j}/c$. We note that (10) appears to be new, but we have checked its validity against numerics[39] and also known expressions in the limit ($d \to \infty$) of an isolated sphere.[40] We also note that the factors of $\operatorname{Im} \epsilon_G / \operatorname{Im} \epsilon_1$ in both flux expressions arise because we only consider fluctuations arising from the active constituents.

We begin our analysis by first considering general radiative features of dimers, comprising spheres of constant (dispersionless) dielectric permittivities $\epsilon_{1,2}$ and equal radii R, which very clearly delineate the operating conditions needed to observe $\Phi_{12} \gg \Phi_0$. We assume that one of the spheres
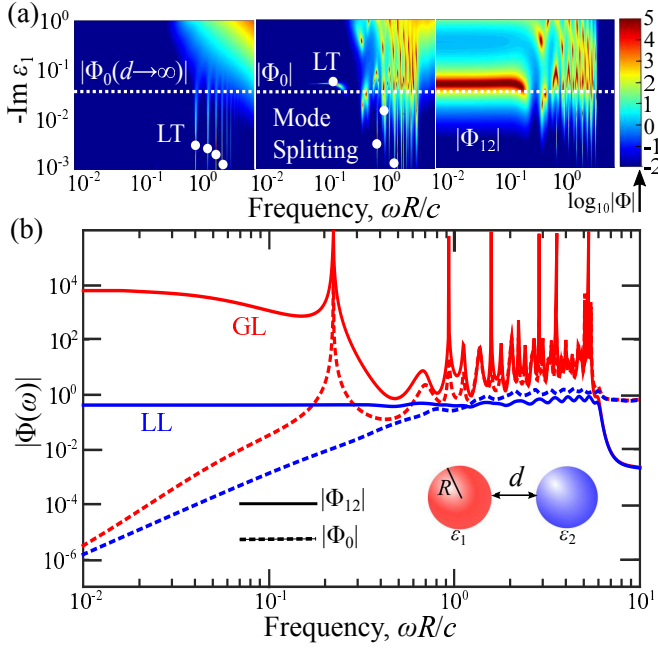
FIG. 3. Far-field flux $\Phi_0(\omega)$ and flux-transfer $\Phi_{12}(\omega)$ associated with a dimer of two spheres of equal radii R, permittivities $\epsilon_1 = \epsilon_r + \epsilon_G$ and $\epsilon_2 = \epsilon_r$, with $\mathrm{Im}\,\epsilon_r = 0.05$, and separated by distance of separation d, under various operating conditions. (a) Dependence of $\Phi_0(\omega)$ and $\Phi_{12}(\omega)$ on $\mathrm{Im}\,\epsilon_1 < 0$ (under gain) at fixed $\mathrm{Re}\,\epsilon_{1,2} = -1.522$, and for either $d \to \infty$ (left) or $d/R = 0.3$ (middle/right). White circles indicate the lasing threshold of a few individual modes while white dashed lines indicate operating parameters (cross sections) for the plots in (b), which show Φ_{12} (solid lines) and Φ_0 (dashed lines) at fixed $\mathrm{Im}\,\epsilon_1 = -\mathrm{Im}\,\epsilon_2 = -0.05$ and $d/R = 0.3$. The plots compare the flux rates of gain-loss (GL) dimers (red lines) against those of passive (LL) dimers (blue lines).

(with dielectric ϵ_1) is doped with a gain medium such that $\mathrm{Im}\,\epsilon_1 < 0$ The top contour in Fig. 3(a) shows Φ_0 from an isolated sphere of $\mathrm{Re}\,\epsilon = -1.522$ as a function of gain permittivity $\mathrm{Im}\,\epsilon_1$, illustrating the appearance of Mie resonances and consequently, ASE peaks occurring at $k_0 R \gtrsim 1$. As expected, the LTs (white circles indicate a select few) associated with each resonance occur at those values of gain where (as in the planar case) $\Phi_0 \to \infty$ and the mode bandwidths $\to 0$, decreasing with increasing $k_0 R$ (smaller radiative losses). Note that these divergences are obscured in the contour plot by our finite numerical resolution, which sets an upper bound on Φ_0. The middle contour plot in Fig. 3(a) shows that a passive sphere with $\mathrm{Im}\,\epsilon_2 = 0.05$ in proximity to the gain sphere ($d/R = 0.3$) causes the Mie resonances to couple and split, leading to dramatic changes in the corresponding LTs. Noticeably, while the presence of the lossy sphere introduces additional dissipative channels, in some cases it can nevertheless enhance ASE (decreasing LTs) by suppressing radiative losses.[43] These results are well-studied in the literature[18,43] but they are important here because our linear FDT is only valid below LT. Another feature associated with such dimers is the significant enhancement in Φ_{12} compared to Φ_0 in the subwavelength regime $k_0 R \ll 1$,[44,45] illustrated by the mid-

dle/right contours of Fig. 3(a). Note that while such near-field enhancements have been studied extensively in the context of passive bodies,[4,7,45] as we show here, the introduction of gain can lead to even further enhancements. This is demonstrated by the flux spectra in Fig. 3(b) (corresponding to slices of the contour maps, denoted by white dashed lines), which compare the flux rates of both active (red lines) and passive (blue lines) dimers. The spectra indicate that, while the large radiative components of Mie resonances at intermediate and large frequencies $k_0 R \gtrsim 1$ lead to roughly equal enhancements in Φ_{12} and $\Phi_0 \sim \Phi_{12}$, the saturating and dominant contribution of evanescent fields and the presence of surface–plasmon resonances in the long wavelength regime cause $\Phi_0 \to 0$ and $\Phi_{12} \gg 1$ as $\omega \to 0$. As expected, the existence and coupling of these resonances depend sensitively on d/R, arising at $\mathrm{Re}\,\epsilon \approx \{-2, -1\}$ in the limit $d \to \{0, \infty\}$ of two semi-infinite plates or isolated spheres, respectively.

B. Dipolar approximation

Since the subwavelength regime allows $\Phi_{12} \gg \Phi_0$, we employ a simple dipolar approximation (DA)[46,47] or quasistatic analysis to understand these enhancements in more detail. In the quasistatic regime, treating the spheres as point dipoles, we find that the corresponding flux rates are given by:

$$\Phi_{12} = \frac{12\,\mathrm{Im}\,\epsilon_G}{\pi L^6\,\mathrm{Im}\,\epsilon_1}\,\mathrm{Im}\,\alpha_1^{\mathrm{eff}}\,\mathrm{Im}\,\alpha_2^{\mathrm{eff}} \tag{11}$$

$$\Phi_0 = \frac{4\,\mathrm{Im}\,\epsilon_G}{\pi\,\mathrm{Im}\,\epsilon_1}(k_0 R)^3\,\mathrm{Im}\,\alpha_1^{\mathrm{eff}}, \tag{12}$$

where α_i^{eff} denote each spheres' effective *anisotropic* polarizability (computed by taking into account induced polarization of the dipoles), with parallel ($\parallel$) and perpendicular ($\perp$) components given by:[48]

$$\alpha_{\perp,1/2}^{\mathrm{eff}} = \alpha_{1/2}\frac{1 - \frac{\alpha_{2/1}}{L^3}}{1 - \frac{\alpha_1\alpha_2}{L^6}}, \quad \alpha_{\parallel,1/2}^{\mathrm{eff}} = \alpha_{1/2}\frac{1 + \frac{2\alpha_{2/1}}{L^3}}{1 - \frac{4\alpha_1\alpha_2}{L^6}} \tag{13}$$

with $\alpha_i = \frac{\epsilon_i - 1}{\epsilon_i + 2}$ denoting the vacuum polarizability of the isolated spheres in units of $4\pi R^3$ and $L = 2 + \frac{d}{R}$ their center-center distance in units of R.

It is well known that in the far-field dipolar limit $d/R \gg 1$, both $\Phi_{12}, \Phi_0 \to \infty$ under the resonance condition, $\mathrm{Re}\,\epsilon = -2$ and zero material loss $\mathrm{Im}\,\epsilon \to 0$.[10,44,46] At smaller separations, these two conditions are modified to $|L^6 - \alpha_1\alpha_2| = 0$ ($\parallel$ component) or $|L^6 - 4\alpha_1\alpha_2| = 0$ ($\perp$ component) due to changes in the effective polarizability of each sphere. It follows that for a passive dimer, while this affects the resonance condition $\mathrm{Re}\,\epsilon = -2$, the divergence can be reached only when both $\mathrm{Im}\,\epsilon_i \to 0$. For instance, in passive dimers with $\alpha = \alpha_1 = \alpha_2$, $\mathrm{Im}\,\alpha^{\mathrm{eff}} \to \infty$ at specific $L^3 = -\mathrm{Re}\,\alpha$ ($\perp$ component) and $L^3 = 2\,\mathrm{Re}\,\alpha$ ($\parallel$ component) for $\mathrm{Re}\,\epsilon$ close to -2 but only under the condition of zero loss, illustrated in the top contour of Fig. 4(a) for a small $\mathrm{Im}\,\epsilon_{1,2} = 0.01$. Of course, it is well known that these quasistatic conditions cannot generally be satisfied in finite, passive geometries, resulting in finite flux rates (even in the limit as $\mathrm{Im}\,\epsilon \to 0$);
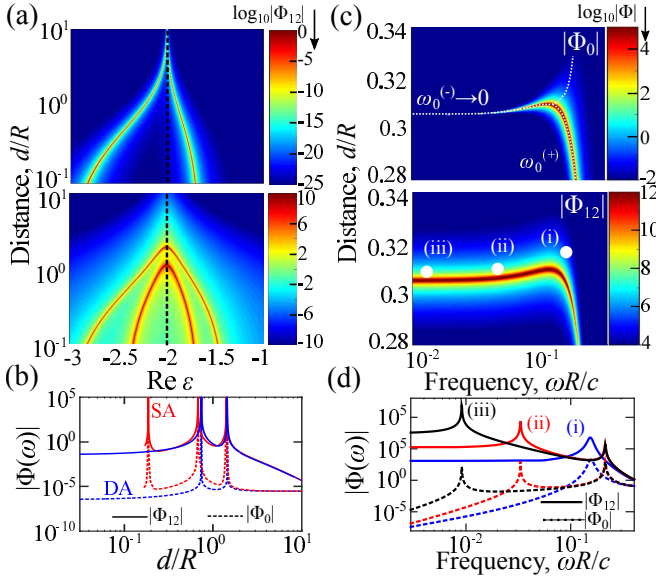
FIG. 4. (a) Flux-transfer rate Φ_{12} associated with the sphere dimer system of Fig. 3 under a simple dipolar approximation (DA), in either passive ($\mathrm{Im}\,\epsilon_{1,2} = 0.01$, top) or active ($\mathrm{Im}\,\epsilon_1 = -\mathrm{Im}\,\epsilon_2 = -0.1$, bottom) regimes, as a function of $\mathrm{Re}\,\epsilon_{1,2}$ and d/R. While the flux rate diverges in the active case under total loss compensation, only the rate per unit volume diverges in the case of finite, passive spheres. The validity of the DA for large $d > R$ is illustrated in (b), which shows also results obtained using the semi-analytical (SA) equations [(9) and (10)]. (c) Flux rate spectra $\Phi_0(\omega)$ (top) and $\Phi_{12}(\omega)$ (bottom) of the dimer system under the $\mathcal{PT}$ symmetry condition, $\mathrm{Re}\,\epsilon_{1,2} = -1.522$ and $\mathrm{Im}\,\epsilon_1 = -\mathrm{Im}\,\epsilon_2 = -0.05$, illustrating the splitting of a sub-wavelength dimer mode as d changes around a critical $d_c \approx 0.306R$. The two branches include both quasistatic $\omega_0^{(-)}$ and subwavelength $\omega_0^{(+)}$ resonances. (d) Flux spectra at three different separations $d \approx \{0.3056, 0.302, 0.3017\}R$, marked by the white dots (i), (ii), and (iii), respectively, in the bottom contour in (c).

essentially, two far-separated ($d \to \infty$) spheres will not behave as quasistatic dipoles owing to their finite skin-depth, except in the limit $R \to 0$ in which case only the flux rates per unit volume rather than the absolute rates diverge.[10,49] Gain–loss dimers, on the other hand, exhibit diverging flux rates (i.e. they can lase) under finite material gain and loss rates, as well as in finite geometries that fall outside of the quasistatic regime. A clear and practical example are objects satisfying the so-called parity-time ($\mathcal{PT}$) symmetry condition, $\epsilon_1 = \epsilon_2^*$ or $\alpha = \alpha_1 = \alpha_2^*$ (assuming equal radii). In this case, the dipolar analysis above suggests a divergence at the critical separation d_c corresponding to $L^3 = \{|\alpha|, \sqrt{2}|\alpha|\}$, illustrated in the bottom contour plot of Fig. 3(c), assuming $|\mathrm{Im}\,\epsilon_{1,2}| = 0.1$. It also follows that under finite loss rates $\mathrm{Im}\,\alpha \neq 0$, the emission from gain–loss dimers can be made arbitrarily larger than that of their passive counterparts. Note that in order to capture the enhancement factor associated with active dimers, the induced polarization effect (captured by our quasistatic analysis to first order in d/R) must be included, emphasizing the importance of geometry along with gain in realizing maximum ASET; the former has a significantly smaller effect on passive dimers.

Deviations from zero-loss conditions lead to different scalings in active versus passive dimers: for small but finite $\mathrm{Im}\,\alpha \ll |\mathrm{Re}\,\alpha|$, the passive transfer rate, $\Phi_{12} \sim (\frac{\mathrm{Re}\,\alpha}{\mathrm{Im}\,\alpha})^2$, illustrating a significantly more dramatic increase in flux rates with decreasing losses than is otherwise observed in the planar geometry discussed above.[11] Additional enhancements arise in active dimers. For instance, under an equally small breaking of $\mathcal{PT}$ symmetry in our example above, i.e. $\alpha = \alpha_1 = \alpha_2^* + i\delta$, one finds that $\Phi_{12} \sim (\frac{\mathrm{Im}\,\alpha}{\mathrm{Re}\,\alpha})^2(\frac{\mathrm{Im}\,\alpha}{\delta})^2$. Considering the typically large loss rates of metals near the plasma frequency, i.e. $\mathrm{Im}\,\alpha/\mathrm{Re}\,\alpha \sim 1$, it is clear that one can achieve larger enhancement factors in active dimers as compared to passive dimers. Note that although we focus here on a $\mathcal{PT}$-symmetric configuration as a convenient illustration of the divergence phenomenon, similar results arise under different scenarios, as described by the divergence condition above.

While the DA offers intuitive and analytical insights into energy exchange in the subwavelength regime, it fails to capture many important, finite-size effects that result from second- and higher-order scattering artifacts, and must therefore be supplemented by exact calculations if more quantitative predictions are desired. Nevertheless, as shown in Fig. 4(b), when compared against the SA above, with flux rates given by (9) and (10), the DA and exact predictions exhibit close agreement whenever $d \gtrsim R$, suggesting that the DA is sufficient to understand the main features of energy transfer at intermediate to large separations. It further follows from the DA that the ratio of ASET to ASE, $\frac{\Phi_{12}}{\Phi_0} \sim \frac{(R/d)^6}{(k_0 R)^3}$, favoring absorption to radiation as $k_0 R \to 0$, clearly evident in Fig. 4. Furthermore, although our dipolar analysis suggests a unique L at which $\Phi_{12} \to \infty$, finite geometries support many such modes and there exists multiple critical separations and quasistatic divergences, an example of which is demonstrated in Fig. 4(b)(c), which delineate lasing transitions and strong, distance-dependent enhancements at $d \lesssim R$ that are not predicted by DA. In particular, Fig. 4(c) shows the flux rates under $\mathcal{PT}$ symmetry, corresponding to $\mathrm{Re}\,\epsilon = -1.522$ and $\mathrm{Im}\,\epsilon_1 = -\mathrm{Im}\,\epsilon_2 = -0.05$, illustrating the appearance of a subwavelength resonance (otherwise absent at far-away separations) at $d \approx 0.317R$ and $\omega_0 R/c \approx 0.25$ that splits into two resonances at $d/R \approx 0.306R$, whose frequencies $\omega_0^\pm$ move farther apart (white dashed lines in the top contour plot) with decreasing d. Such a resonant coupling mechanism results in an ultra-large red shift $\omega_0^- \to 0$ of one of the branches, as $d \to d_c$, eventually leading to the quasistatic divergence predicted by the dipolar analysis and better illustrated in the bottom figure of Fig. 4(c), which shows the spectrum corresponding to three different separations, denoted by white dots. While the DA does not predict such a low-d divergence, which arises due to higher-order scattering effects, it does predict the right scaling of Φ_{12}/Φ_0 with the various parameters.

The analysis above suggests that a proper combination of gain, geometry, and subwavelength operating conditions can provide optimal conditions for achieving ASET $\gg$ ASE below the LT. In what follows, we consider a more practical and interesting, extended geometry, involving lattices of spheres that exchange energy among one another, where one can potentially observe even larger enhancements, leaving open the
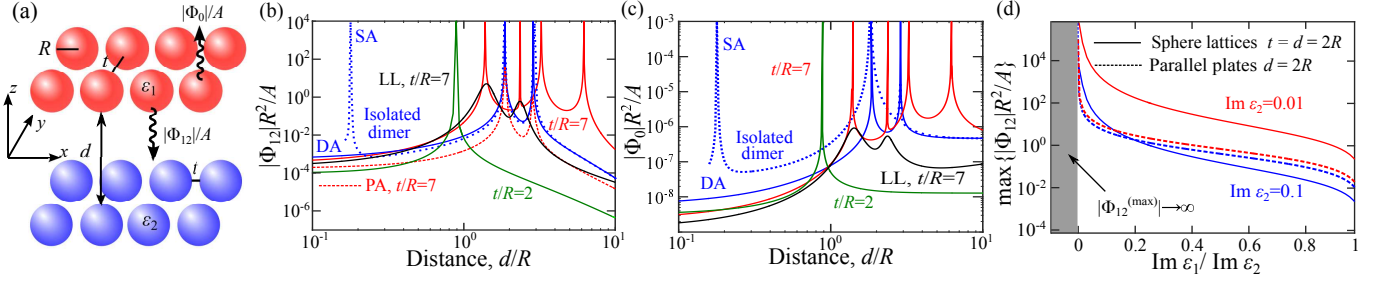
FIG. 5. (b) Flux transfer $|\Phi_{12}|R^2/A$ and (c) far-field flux $|\Phi_0|R^2/A$ associated with the system shown schematically in (a), involving an infinite, two-dimensional lattices of gain and loss spheres of equal radii R and period $t \approx d$, and separated by a (varying) vertical distance d, for different choices of $t/R \gtrsim 1$ and fixed values of $\mathrm{Re}\,\epsilon = -1.95$ and $\mathrm{Im}\,\epsilon_1 = -\mathrm{Im}\,\epsilon_2 = -0.01$. Also shown are the corresponding flux rates obtained using a simple pairwise approximation (PA, dashed red lines) that ignores multiple scattering (see text), or associated with either passive spheres (LL, black solid lines) or isolated dimers (blue lines, both DA and SA). The flux rates are normalized by either the dimensionless unit areas A/R^2 in the case of lattices, with $A = (t + 2R)^2$, or $A = 4\pi R^2$ in the case of an isolated dimer. (d) compares the maximum achievable flux rate $|\Phi_{12}|R^2/A$ in sphere lattice (solid lines) versus planar (dashed lines) geometries as a function of the ratio $\mathrm{Im}\,\epsilon_1/\mathrm{Im}\,\epsilon_2$ (relative overall permittivity of the gain spheres/plates) for two different choices of $\mathrm{Im}\,\epsilon_2 = \{0.01, 0.1\}$ (red, blue) and fixed lattice parameters $d/R = t/R = 2$.

possibility of further improvements in other geometries.[50–52] Because exact calculations of flux rates in such a structure are far more complicated,[53] we restrict ourselves to quasistatic situations that lie within the scope of our DA.

C. Sphere lattices

The combination of reduced loss rates and resonant, near-field enhancements potentially achievable in extended geometries could lead to orders of magnitude larger heat flux rates compared to planar geometries. In fact, as we showed recently in Ref. 11, structures comprising tightly packed, pariwise-additive dipolar radiators can approach the fundamental limits of radiative energy exchange imposed by energy conservation. In what follows, we analyze more realistic versions of such structures, albeit under gain, demonstrating the possibility of achieving significant and widely tunable near-field and material flux enhancements.

We consider two vacuum-separated square lattices of gain–loss nanospheres having equal radii R, lattice spacing t, and surface–surface separation d, depicted in Fig. 5(a). As noted above, the radiation between and from such structures will, to lower order in $\{d, t\}/R$, depend on the local corrections to the polarizabilities of each individual sphere. The generalization of the DA to consider such a situation yields the following set

of equations for the effective polarizabilities of each sphere:

$$
\left[\frac{1}{\alpha_{G,z}^{(0)}} - \frac{1}{(2+t/R)^3} \sum_{\substack{n_1,n_2=0 \\ n_1+n_2 \neq 0}}^{\infty} \frac{1}{(n_1^2 + n_2^2)^{3/2}} \right] \alpha_{G,z}^{\mathrm{eff}}
$$
$$
- \left[\frac{1}{(2+t/R)^3} \sum_{n_1,n_2=0}^{\infty} \frac{n_1^2 + n_2^2 - 2(d/t)^2}{[n_1^2 + n_2^2 + (d/t)^2]^{5/2}} \right] \alpha_{L,z}^{\mathrm{eff}} = 1
$$
(14)

$$
\left[\frac{1}{\alpha_{G,\|}^{(0)}} - \frac{1}{(2+t/R)^3} \sum_{\substack{n_1=0,n_2=0 \\ n_1+n_2 \neq 0}}^{\infty} \frac{n_2^2 - 11n_1^2}{(n_1^2 + n_2^2)^{5/2}} \right] \alpha_{G,\|}^{\mathrm{eff}}
$$
$$
- \left[\frac{1}{(2+t/R)^3} \sum_{n_1,n_2=0}^{\infty} \frac{(d/t)^2 + n_2^2 - 11n_1^2}{[n_1^2 + n_2^2 + (d/t)^2]^{5/2}} \right] \alpha_{L,\|}^{\mathrm{eff}} = 1,
$$
(15)

in terms of the bare polarizabilities $\alpha_{G,L}^{(0)}$ and structure parameters. (Note that there are three additional equations, which we have chosen to omit, obtained by letting $G \leftrightarrow L$ above.)

Figure 5 shows (b) Φ_{12} and (c) Φ_0 in the subwavelength regime $k_0 R = 0.01$, normalized by the dimensionless lattice area $A/R^2 = (2 + t/R)^2$, assuming spheres of $\epsilon_{1,2} = -1.95 \pm 0.01i$ and for various $t = \{2, 7\}R$. To understand the range of validity of the DA with respect to d/R, we once again compare its predictions against our semi-analytical formulas (SA) in the case of isolated dimers (dotted blue lines), showing excellent agreement in the range $d/R > 1$; note, however, the failure of DA to predict the additional peak at low $d/R \approx 0.2$. Restricting our analysis to large separations, one finds that the presence of additional spheres causes significant enhancements and modifications to the flux rates, leading to complicated, non-monotonic dependences on geometric parameters such as t. To illustrate the importance of multiple-scattering among many particles, we also show re-

sults obtained using a simple pairwise-additive (PA) approximation (dashed lines), in which the flux rates associated with pairs of spheres are individually summed.

Figure 5(d) compares the performance of sphere lattices against that of parallel plates, showing the maximum achievable $|\Phi_{12}|/(A/R^2)$ as a function of relative active medium permittivity $\operatorname{Im}\epsilon_1/\operatorname{Im}\epsilon_2$ for fixed $d/R = t/R = 2$ and multiple loss rates $\operatorname{Im}\epsilon_2 = \{0.01, 0.1\}$ (red and blue lines), varying $\operatorname{Re}\epsilon_{1,2}$ so as to satisfy the resonant condition. As noted above, for $\operatorname{Im}\epsilon_1 < 0$ (loss compensation), it is always possible to choose geometric parameters under which the system undergoes lasing (gray shaded region), though this condition can only be obtained analytically for simple structures such as the plates or dipolar spheres above. Below the LT, it is evident that there is significant enhancement in ASET in the case of sphere lattices compared to plates, especially as the lattice system approaches the LT. Such an enhancement depends crucially on the loss rates, decreasing with increasing $\operatorname{Im}\epsilon_2$, which can be explained by the weak, logarithmic dependence of the planar flux rates on overall loss compensation.[11] Note that as discussed above, at finite R, the DA becomes increasingly inaccurate in the limit $\operatorname{Im}\epsilon_1 \to 0$, owing to the finite skin depth effect.[10,49] Our calculations therefore offer only a qualitative understanding of the trade-offs in exploiting particle lattices as opposed to plates. Under losses $\operatorname{Im}\epsilon_2 \approx 0.1$ typical of plasmonic materials, we find that parallel plates exchange more energy compared to sphere lattices for a wide range of gain parameters (except close to the LT), while the latter dominate at smaller $\operatorname{Im}\epsilon_2$ and can be greatly enhanced by the presence of even a small amount of gain. Note that while we have chosen to investigate only the case $\{t, d\}/R = 2$ in order to ensure the validity of the DA, potentially larger enhancements are expected to arise at shorter distances or lattice separations, but such an analysis requires a full treatment of ASET in these extended systems, including both finite size and nonlinear effects.[54,55] Nevertheless, our results provide a glimpse of the opportunities for tuning ASET in structured materials.

D. Real materials

The ability to achieve gain at subwavelength frequencies is highly constrained by size and material considerations. In what follows, we describe ASET predictions in a potentially viable material system. Consider a sphere dimer consisting of two ion-doped metallic spheres, shown schematically on the inset of Fig. 6. While there are many material candidates, including various choices of metal-doped oxides and chalcogenides,[56] for illustration, we consider a medium consisting of $(2wt\%)$ Ga-doped zinc oxide (GZO) that is further doped with 4-level Chromium (Cr^{2+}) ions, in which case the transition wavelength lies in the near infrared. The permittivity and gain profile of the ions and GZO are well described by (2), with $\omega_{21} = 0.75 \times 10^{15}$ rad/s, $\gamma_\perp \approx 0.02\omega_{21}$, and,[56–58]

$$\epsilon_r(\omega) = \epsilon_\infty - \frac{\omega_p^2}{\omega(\omega + i\Gamma_p)} + \frac{f_1\omega_1^2}{\omega_1^2 - \omega^2 - i\omega\Gamma_1} \quad (16)$$
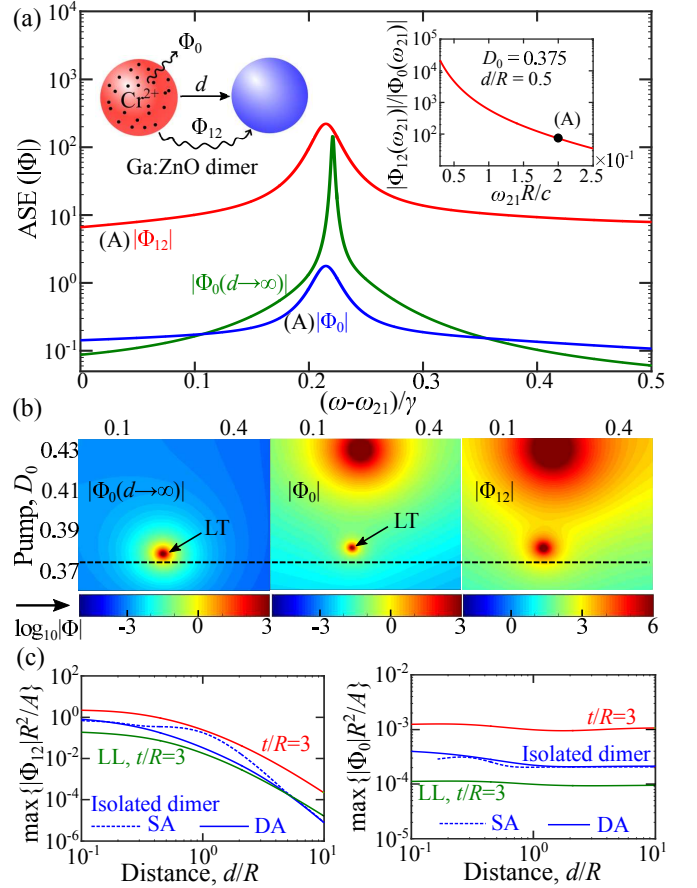

FIG. 6. (a) Far-field flux $\Phi_0(\omega)$ (blue line) and flux-transfer $\Phi_{12}(\omega)$ (red line) spectra of a dimer consisting of two Ga-doped zinc-oxide spheres of radii $R = 0.2c/\omega_{21}$, separated by a distance $d/R = 0.5$. One of the spheres is doped with Chromium (Cr^{2+}) ions having transition wavelength $\lambda_{21} = 2.51\mu$m, and pumped to a population inversion $D_0 = 0.375$ ($\hbar\gamma_\perp/4\pi^2 g^2$). Also shown is the far-field emission $\Phi_0(d \to \infty)$ of the isolated gain sphere (green line). The top inset shows the peak ratio $\Phi_{12}^{max}/\Phi_0^{max}$ with respect to changes in R, keeping d/R and D_0 fixed. (b) Contour plots illustrating variations in Φ_0 (left/middle) and Φ_{12} (right) with respect to D_0, with the black dashed lines indicating operating parameters in (a). (c) Maximum spectral flux rates $|\Phi_{12}(\omega)|R^2/A$ (left) and $|\Phi_0(\omega)|R^2/A$ (right) for extended sphere lattices comprising GZO gain-loss spheres operating at $D_0 = 0.3$ ($\hbar\gamma_\perp/4\pi^2 g^2$), well below the LT, but of radii $R \sim 0.05c/\omega_{21}$, as a function of d/R and for different values of t/R. Also shown are the flux rates of passive lattices (LL, black solid lines), obtained by letting $D_0 = 0$.

where $\epsilon_\infty = 2.475$, $f_1 = 0.866$, $\omega_p = 2.23\omega_{21}$, $\Gamma_p = 0.0345\omega_p$, $\omega_1 = 9.82\omega_{21}$, and $\Gamma_1 = 0.006\omega_1$. These parameters dictate dimer sizes and configurations needed to operate in the subwavelength regime.

Figure 6(a) shows Φ_{12} (red line) and Φ_0 (blue line) for one possible dimer configuration, corresponding to $R = 0.2c/\omega_{21} \approx 80$nm, $d/R = 0.5$, and population inversion $D_0 = 0.375$ ($\hbar\gamma_\perp/4\pi g^2$), demonstrating orders of magnitude larger ASET compared to ASE within the gain bandwidth. Noticeably, the emission from an isolated sphere under the same gain parameters (green line) is significantly

larger, evidence of an increased LT due to the presence of the lossy sphere. The flux spectra of this system are explored in Fig. 6(b) with respect to changes in D_0, illustrating the appearance of the subwavelength peak and large $\Phi_{12} \gg 1$. As expected, the LT corresponding to the first peak occurs slightly above $\text{Im}\,\epsilon_L \approx 0.37$, which is the threshold gain needed to compensate material loss, at which point $\text{Im}\,\epsilon_1 < 0$. The black dashed lines in the contours denote the operating parameters of Fig. 6(a), confirming that the system lies below the LT. As expected, smaller dimers lead to larger $\frac{\Phi_{12}}{\Phi_0} \sim (k_0 R)^{-3}$, as illustrated by the top inset of Fig. 6(a). Figure 6(c) shows the flux rates (red and blue lines) corresponding to extended lattices of spheres comprising the same GZO gain–loss profiles and with radii $R = 0.05c/\omega_{21} \approx 20\text{nm}$ (in the highly subwavelength regime), in a situation where the system is well below the LT, which occurs at $D_0 = 0.3\,(\hbar\gamma_\perp/4\pi^2 g^2)$. Noticeably, the flux rates are significantly larger than the rates achievable in passive structures (green solid lines).

III. CONCLUDING REMARKS

Our predictions shed light on considerations needed to achieve large ASET between structured active–passive materials, attained via a combination of loss compensation in conjunction with near-field effects. While our work follows closely well-known and related ideas in the areas of near-field heat transport and nano-scale lasers (e.g. spacers), the possibility of tuning and enhancing heat among active bodies in the near field is only starting to be explored.[26,59] Our analysis, while motivating and correct in regimes where ASE domiantes stimulated emission, ignores important nonlinear and radiative-feedback effects present in gain media as the LT is approached, nor have we considered specific pump mechanisms which will necessarily affect power requirements and ASET predictions,[60,61] especially above threshold. To answer such questions, future analyses based on full solution of the Maxwell–Bloch equations[62,63] or variants thereof[35,58] are needed.

Appendix A: Vector spherical harmonics

When deriving the flux rates associated with two spheres, we employed the following spherical-vector functions:

$$\mathbf{M}_{\ell m}^{(p)+}(k\mathbf{x}) = z_\ell^{(p)}(kr)\mathbf{V}_{\ell m}^{(2)}(\theta,\phi), \tag{A1}$$

$$\mathbf{M}_{\ell m}^{(p)-}(k\mathbf{x}) = \zeta_\ell^{(p)}(kr)\mathbf{V}_{\ell m}^{(3)}(\theta,\phi) + \frac{z_\ell^{(p)}(kr)}{kr}\sqrt{\ell(\ell+1)}\mathbf{V}_{\ell m}^{(1)}(\theta,\phi), \tag{A2}$$

where $z_\ell^{(p)}$ are spherical Bessel ($p=1$) and Hankel ($p=3$) functions of order ℓ, $\zeta_\ell^{(p)}(x) = \frac{1}{x}\frac{d}{dx}[xz_\ell^{(p)}(x)]$, and $\mathbf{V}_{\ell m}^{(p)}$ and associated spherical vector harmonics,[42]

$$\mathbf{V}_{\ell m}^{(1)}(\theta,\phi) = \hat{\mathbf{r}}Y_{\ell m} \tag{A3}$$

$$\mathbf{V}_{\ell m}^{(2)}(\theta,\phi) = \frac{1}{\sqrt{\ell(\ell+1)}}\left(-\hat{\phi}\frac{\partial Y_{\ell m}}{\partial\theta} + i\hat{\theta}\frac{m}{\sin\theta}Y_{\ell m}\right) \tag{A4}$$

$$\mathbf{V}^{(3)}(\theta,\phi) = \frac{1}{\sqrt{\ell(\ell+1)}}\left(\hat{\theta}\frac{\partial Y_{\ell m}}{\partial\theta} + i\hat{\phi}\frac{m}{\sin\theta}Y_{\ell m}\right), \tag{A5}$$

which satisfy the following orthogonality relations:

$$\oint_S \mathbf{V}_{\ell m}^{(p)}\cdot\mathbf{V}_{\ell'm'}^{(p')*} = \delta_{\ell\ell'}\delta_{pp'}\delta_{mm'}$$

$$\oint_S d\Omega\,\mathbf{V}_{\ell m}^{(p)}\times\mathbf{V}_{\ell'm'}^{(p)*}\cdot\hat{\mathbf{r}} = -\oint_S d\Omega\,\mathbf{V}_{\ell m}^{(2)}\times\mathbf{V}_{\ell'm'}^{(3)*}\cdot\hat{\mathbf{r}}$$
$$= \delta_{\ell\ell'}\delta_{mm'}$$

$$\int_{V_i} d\mathbf{x}'\,\mathbf{M}_{\ell m}^{(1)+}(k\mathbf{x}')\cdot\mathbf{M}_{\ell'm'}^{(1)+*}(k\mathbf{x}')$$
$$= R_i^2\,\text{Im}\left[k_i^* z_\ell^{(1)}(k_iR_i)\zeta_\ell^{(1)*}(k_iR_i)\right]\frac{\delta_{\ell\ell'}\delta_{mm'}}{k_0^2\,\text{Im}\,\epsilon_i},$$

$$\int_{V_i} d\mathbf{x}'\,\mathbf{M}_{\ell m}^{(1)-}(k\mathbf{x}')\cdot\mathbf{M}_{\ell'm'}^{(1)-*}(k\mathbf{x}')$$
$$= R_i^2\,\text{Im}\left[k_i^* z_\ell^{(1)*}(k_iR_i)\zeta_\ell^{(1)}(k_iR_i)\right]\frac{\delta_{\ell\ell'}\delta_{mm'}}{k_0^2\,\text{Im}\,\epsilon_i}.$$

[1] R.S Ottens, V. Quetschke, Stay Wise, A.A. Alemi, R. Lundock, G. Mueller, D.H. Reitze, D.B. Tanner, and B.F. Whiting. Near-field radiative heat transfer between macroscopic planar surfaces. *Phys. Rev. Lett.*, 107:014301, 2011.

[2] O Ilic, M. Jablan, J. D. Joannopoulos, I. Celanovic, Hrovje Buljan, and Marin Soljacic. Near-field thermal radiation transfer controlled by plasmons in graphene. *Phys. Rev. B*, 85:155422, 2012.

[3] Mathieu Francoeur, M. Pinar Menguc, and Dodolphe Vaillon. Near-field radiative heat transfer enhancement via surface phonon polaritons coupling in thin films. *Appl. Phys. Lett.*, 93:043109, 2008.

[4] S. Basu, Z. M. Zhang, and C. J. Fu. Review of near-field thermal radiation and its application to energy conversion. *Int. J. Energy Res.*, 33(13):1203–1232, 2009.

[5] Jackson J. Loomis and Humphrey J. Maris. Theory of heat transfer by evanescent electromagnetic waves. *Phys. Rev. B*, 50:18517–18524, 1994.

[6] S. A. Biehs, F. S. S. Rosa, and P. Ben-Abdallah. Modulation of near-field heat transfer between two gratings. *Appl. Phys. Lett.*, 98(24):243102, 2011.

[7] Philippe Ben-Abdallah, Karl Joulain, Jeremie Drevillon, and Gilberto Domingues. Near-field heat transfer mediated by surface wave hybridization between two films. *J. Appl. Phys.*, 106(4), 044306 2009.

[8] Arvind Narayanaswamy and Gang Chen. Thermal near-field radiative transfer between two spheres. *Phys. Rev. B*, 77(7):075125, 2008.

[9] A. Narayanaswamy, S. Shen, and G. Chen. Near-field radiative heat transfer between a sphere and a substrate. *Phys. Rev. B*, 78:115303, 2008.

[10] Owen D Miller, Athanasios G Polimeridis, MT Homer Reid, Chia Wei Hsu, Brendan G DeLacy, John D Joannopoulos, Marin Soljačić, and Steven G Johnson. Fundamental limits to optical response in absorptive systems. *Optics express*, 24(4):3329–3364, 2016.

[11] Owen D Miller, Steven G Johnson, and Alejandro W Rodriguez. Shape-independent limits to near-field radiative heat transfer. *Physical Review Letters*, 115(20):204302, 2015.

[12] A. Guo, G.J. Salamo, D. Duchesne, R. Morandotti, M. Voltaier-Ravat, V Aimez, G.A. Sivilglou, and D.N. Christodoulides. Observation of $\mathcal{PT}$-symmetry breaking in complex optical potentials. *Phys. Rev. Lett.*, 103:093902, 2009.

[13] H. Wenzel, U. Bandelow, H. Wunsche, and J. Rehberg. Mechanisms of fast self pulsations in two-section dfb lasers. *IEEE J. of Quantum Electronics*, 32:69–78, 1996.

[14] Z. Lin, H. Ramezani, T. Eichelkraut, T. Kottos, H. Cao, and D.N. Christodoulides. Unidirectional invisibility induced by $\mathcal{PT}-$symmetric periodic structures. *Phys. Rev. Lett.*, 106:213901, 2011.

[15] B. Peng, S. Ozdemir, F. Lei, F. Monifi, M. Gianfreda, G. Long, S. Fan, F. Nori, C. Bender, and L. Yang. Parity-time-symmetric whispering-gallery microcavities. *Nature Physics*, 10:394–398, 2014.

[16] Chinmay Khandekar, Adi Pick, Steven G. Johnson, and Alejandro W. Rodriguez. Radiative heat transfer in nonlinear kerr media. *Phys. Rev. B*, 91:115406, 2015.

[17] Chinmay Khandekar, Zin Lin, and Alejandro W. Rodriguez. Thermal radiation from optically driven kerr ($\chi^{(3)}$) photonic cavities. *Appl. Phys. Lett.*, 106:151109, 2015.

[18] B. Peng, S. Ozdemir, S. Rotter, H. Yilmaz, M. Liertzer, F. Monifi, C.M. Bender, F. Nori, and L. Yang. Loss-induced suppression and revival of lasing. *Science*, 17:328–332, 2014.

[19] X.L. Liu, R.Z. Zhang, and Z.M. Zhang. Near-field radiative heat transfer with doped-silicon nanostructred metamaterials. *International Journal of Heat and Mass Transfer*, 73:389–398, 2014.

[20] Philippe Ben-Abdallah and Svend-Age Biehs. Phase-change radiative thermal diode. *Appl. Phys. Lett.*, 103:191907, 2013.

[21] Yue Yang, Soumyadipta Basu, and Liping Wang. Radiation-based near-field thermal rectification with phase transition materials. *Appl. Phys. Lett.*, 103:163101, 2013.

[22] T. Ijiro and N. Yamada. Near-field radiative heat transfer between two parallel sio_2 plates with and without microcavities. *Appl. Phys. Lett.*, 106:023103, 2015.

[23] A.W. Rodriguez, Ognjen Illic, P. Bermel, I. Celanovic, J.D. Joannopoulos, M. Solijacic, and S.G. Johnson. Frequency-selective near-field radiative heat transfer between photonic crystal slabs: a computational approach for arbitrary geometries and materials. *Phys. Rev. Lett.*, 107:114302, 2011.

[24] B. Song, Y. Ganjeh, S. Sadat, D. Thompson, A. Fiorino, V. Fernandez-Hurtado, J. Feist, J.Garcia Vidal, J. C. Cuevas, P. Reddy, and E. Meyhofer. Enhancement of near-field radiative heat transfer using polar dielectric thin films. *Nature Nanotechnology*, 10:235–238, 2015.

[25] Yi Huang, Svetlana V. Borishkina, and Gang Chen. Electrically

[26] tunable near-field radiative heat transfer via ferroelectric materials. *Appl. Phys. Lett.*, 105:244102, 2014.

[26] K. Chen, P. Santhanam, S. Sandhu, L. Zhu, and S. Fan. Heat-flux control and solid-state cooling by regulating chemical potential of photons in near-field electromagnetic heat transfer. *Phys. Rev. B*, 91:134301, 2015.

[27] P.J. van Zwol, L. Ranno, and Chevrier J. Tuning near field radiative heat flux through surface excitations with a metal insulator transition. *Phys. Rev. Lett.*, 108:234301, 2012.

[28] L. Zhu, C.R. Otey, and S. Fan. Negative differential thermal conductance through vacuum. *Appl. Phys. Lett.*, 100:044104, 2012.

[29] S. M. Rytov, V. I. Tatarskii, and Yu. A. Kravtsov. *Principles of Statistical Radiophsics II: Correlation Theory of Random Processes*. Springer-Verlag, 1989.

[30] D. Polder and M. Van Hove. Theory of radiative heat transfer between closely spaced bodies. *Phys. Rev. B*, 4:3303–3314, 1971.

[31] R. Matloob, R. Loudon, M. Artoni, S.M. Barnett, and J. Jeffers. Electromagnetic field quantization in amplifying dielectrics. *Phys. Rev. A*, 55:1623–1633, 1997.

[32] M. Francoeur, M.P. Menguc, and R. Vaillon. Spectral tuning of near-field radiative heat flux between two thin silicon carbide films. *J.Phys.D: Appl. Phys.*, 43:075501, 2010.

[33] R_ Graham and H Haken. Quantum theory of light propagation in a fluctuating laser-active medium. *Zeitschrift für Physik*, 213(5):420–450, 1968.

[34] JR Jeffers, N Imoto, and R Loudon. Quantum optics of traveling-wave attenuators and amplifiers. *Physical Review A*, 47(4):3346, 1993.

[35] Adi Pick, Alex Cerjan, David Liu, Alejandro W. Rodriguez, A.Douglas Stone, D. Chong, Yidong, and Steven G. Johnson. Ab-initio multimode linewidth theory for arbitrary inhomogenous laser cavities. *arXiv:1502.07268*, 2015.

[36] J. Skaar. Fresnel equations nad the refractive index of active media. *Phys. Rev. E*, 73:026605, 2006.

[37] Paul Kinsler. Refractive index and wave vector in passive or active media. *Physical Review A*, 79(2):023839, 2009.

[38] Bertil Nistad and Johannes Skaar. Causality and electromagnetic properties of active media. *Physical Review E*, 78(3):036603, 2008.

[39] Athanasios G. Polimeridis, M.T.H. Reid, Weiliang Jin, Steven G. Johnson, Jacob K. White, and W. Rodriguez, Alejandro. Fluctuating volume-current formulation of electromagnetic fluctuations in inhomogenous media: Incandescence and luminescence in arbitrary geometries. *Phys. Rev. B*, 92:134202, 2015.

[40] C.F. Bohren and D.R. Huffman. *Absorption and scattering of light by small particles*. Wiley-VCH, 1998.

[41] Y.M. Wang and W.C. Chew. Efficient ways to compute the vector addition theorem. *J. Elecromagnetic waves and applications*, 7:651–665, 1993.

[42] Weng Cho Chew. *Waves and fields in inhomogenous media*. Wiley-IEEE Press, 1999.

[43] Stefano Longhi and Giuseppe Della Valle. Loss-induced lasing: new findings in laser theory. *arXiv:1505.03028*, 2015.

[44] Gilberto Domingues, Sebastian Volz, Karl Joulain, and Jean-Jacques Greffet. Heat transfer between two nanoparticles through near field interaction. *Phys. Rev. Lett.*, 94:085901, 2005.

[45] Soumyadipta Basu and Mathieu Francoeur. Maximum near-field radiative heat transfer between thin films. *Appl. Phys. Lett.*, 98:243120, 2011.

[46] Pierre-Olivier Chapuis, Marine Laroche, Sebastian Volz, and Jean-Jacques Greffet. Radiative heat transfer between metallic nanoparticles. *Appl. Phys. Lett.*, 92:201906, 2008.

[47] Karl Joulain, Jean-Philippe Mulet, François Marquier, Rémi Carminati, and Jean-Jacques Greffet. Surface electromagnetic

waves thermally excited: Radiative heat transfer, coherence properties and casimir forces revisited in the near field. *Surface Science Reports*, 57(3):59–112, 2005.

[48] A. Pinchuk and G. Schatz. Anisotropic polarizability tensor of a dimer of nanospheres in the vicinity of a plane substrate. *Nnaotechnology*, 16:2209–2217, 2005.

[49] Yuwen Zhang. Nano/microscale heat transfer, 2007.

[50] Oliver Huth, Felix Rüting, S-A Biehs, and Martin Holthaus. Shape-dependence of near-field heat transfer between a spheroidal nanoparticle and a flat surface. *The European Physical Journal Applied Physics*, 50(01):10603, 2010.

[51] Roberta Incardone, Thorsten Emig, and Matthias Krüger. Heat transfer between anisotropic nanoparticles: Enhancement and switching. *EPL (Europhysics Letters)*, 106(4):41001, 2014.

[52] Arvind Narayanaswamy, Sheng Shen, and Gang Chen. Near-field radiative heat transfer between a sphere and a substrate. *Physical Review B*, 78(11):115303, 2008.

[53] IV Zabkov, Vasilii Vasil'evich Klimov, IV Treshin, and OA Glazov. Plasmon oscillations in a linear cluster of spherical nanoparticles. *Quantum Electronics*, 41(8):742–747, 2011.

[54] Alexander Cerjan, Adi Pick, YD Chong, Steven G Johnson, and A Douglas Stone. Quantitative test of general theories of the intrinsic laser linewidth. *Optics express*, 23(22):28316–28340, 2015.

[55] A. Pick, A. Cerjan, D. Liu, A. W. Rodriguez, A. D. Stone, Y. D. Chong, and S. G. Johnson. *Ab initio* multimode linewidth theory for arbitrary inhomogeneous laser cavities. *Phys. Rev. A*, 91:063806, 2015.

[56] Jongbum Kim, Gururaj V. Naik, Naresh K. Emani, Urcan Guler, and Alexandra Boltasseva. Plasmonic resonances in nanostructured transparent conducting oxide films. *IEEE J. Quantum Electron.*, 19:4601907, 2013.

[57] I. Pirozhenko and A. Lambrecht. Influence of slab thickness on the casimir force. *Phys. Rev. A*, 77:013811, 2008.

[58] A. Cerjan, Y. Chong, L. Ge, and A.D. Stone. Steady-state ab initio laser theory for n-level lasers. *Optics Express*, 20:474–488, 2012.

[59] Ding Ding and Austin J. Minnich. Active thermal extraction of near-field thermal radiation. *arXiv*, 1504.01851, 2015.

[60] Qing Gu, Boris Slutsky, Felipe Vallini, Joseph ST Smalley, Maziar P Nezhad, Newton C Frateschi, and Yeshaiahu Fainman. Purcell effect in sub-wavelength semiconductor lasers. *Optics express*, 21(13):15603–15617, 2013.

[61] Weiliang Jin, Chinmay Khandekar, Adi Pick, Athanasios G. Polimeridis, and Alejandro W. Rodriguez. Amplified and directional spontaneous emission from arbitrary composite bodies:self-consistent treatment of purcell effect below threshold. *arXiv:1510.05694*, 2015.

[62] Marlan O. Scully and Suhail Zubairy. *Quantum Optics*. Cambridge University Press, Cambridge, UK, 1997.

[63] A.E. Siegman. *An introduction to lasers and masers*. McGraw Hill, 1971.